



Nanoscale

Synthesis of monodisperse rod-shaped silica particles through biotemplating of surface-functionalized bacteria

Journal:	<i>Nanoscale</i>
Manuscript ID	NR-COM-01-2020-000669.R1
Article Type:	Communication
Date Submitted by the Author:	27-Feb-2020
Complete List of Authors:	<p>Ping, Hang; State Key Laboratory of Advanced Technology for Materials Synthesis and Processing, Poudel, Lokendra; University of Missouri-Kansas City, Physics and Astronomy Xie, Hao; Wuhan University of Technology, Fang, Weijian; State Key Laboratory of Advanced Technology for Materials Synthesis and Processing, Zou, Zhaoyong; Wuhan University of Technology, ; Max Planck Institute of Colloids and Interfaces, Biomaterials Zhai, Pengcheng; Wuhan University of Technology Wagermaier, Wolfgang; Max Planck Institute of Colloids and Interfaces Fratzl, Peter; Max Planck Institute of Colloids and Interfaces, Biomaterials Wang, Weiming; Wuhan University of Technology, State Key Lab Adv Technol Mat Synth & Proc Wang, Hao; Wuhan University of Technology, The State Key Laboratory of Advanced Technology for Materials Synthesis and Processing O'Reilly, Padraic; Molecular Vista, Ching, Wai-Yim; U. Missouri-Kansas City, Physics Fu, Zhengyi; Wuhan University of Technology, The State Key Laboratory of Advanced Technology for Materials Synthesis and Processing</p>

COMMUNICATION

Synthesis of monodisperse rod-shaped silica particles through biotemplating of surface-functionalized bacteria

Received 00th January 20xx,
Accepted 00th January 20xx

Hang Ping,^{†,‡,ab} Lokendra Poudel,^{‡,c} Hao Xie,^d Weijian Fang,^a Zhaoyong Zou,^a Pengcheng Zhai,^a Wolfgang Wagermaier,^b Peter Fratzl,^b Weimin Wang,^a Hao Wang,^a Padraic O'Reilly,^e Wai-Yim Ching*^c and Zhengyi Fu*^a

DOI: 10.1039/x0xx00000x

Mesoporous silica particles of controlled size and shape are potentially beneficial for many applications, but their usage may be limited by the complex procedure of fabrication. Biotemplating provides a facile approach to synthesize materials with desired shapes. Herein, a bioinspired design principle is adopted through displaying silaffin-derived 5R5 proteins on the surface of *Escherichia coli* by genetic manipulations. The genetically modified *Escherichia coli* provides a three-dimensional template to regulate the synthesis of rod-shaped silica. The silicification is initiated on the cell surface under the functionality of 5R5 proteins and subsequently the inner space is gradually filled. Density functional theory simulation reveals the interfacial interactions between silica precursors and R5 peptides at the atomic scale. There is a large conformation change of this protein during biosilicification. Electrostatic interactions contribute to the high affinity between positively charged residues (Lys4, Arg16, Arg17) and negatively charged tetraethyl orthosilicate. The hydrogen bonds develop between Arg16 (O---H), Arg17 (O---H and N---H) and Leu19 (O---H) residues and the forming silica agglomerates. In addition, the resulting rod-shaped silica copy of the bacteria can transform into mesoporous SiO_x nanorods composed of carbon-coated nanoparticles after carbonization, which is shown to allow superior lithium storage performance.

Introduction

Mesoporous silica particles have attracted widespread attention due to their high surface area, tunable pore size and low costs.¹ They are needed for numerous applications, including energy storage, gas sensors, catalysis and biomedical applications.² However, tailor-made particles with controlled size and shape are difficult to fabricate by conventional procedures.³ Nature provides a huge variety of structures and shapes, which allows the materials to achieve their specific functions.⁴ Learning from structure-forming processes in natural materials enables developing new bioprocess-inspired syntheses.⁵ Biotemplating^{6–8} is a well-known approach that harvests complex shapes from natural systems by transforming these shapes directly into ceramic materials, using a variety of processes. Furthermore, biotemplating processes exhibit the potential being up-scaled using biotechnology approaches.⁹ Biotemplating could be utilized to synthesize materials with nanostructures for various applications. For example, one-dimensional wild type or genetically modified M13 viruses were adopted to synthesize nanomaterials.¹⁰ They can serve as template to control the formation of inorganic materials with nanowire morphology. A. M. Belcher et al. investigated the formation of cobalt manganese oxide nanowires by M13 viruses, which exhibited potential for energy storage electrocatalysts.¹¹ J. Bill et al. utilized aspartic acid modified M13 to direct the formation of ZnO fibers with oriented nanocrystals and a high piezoelectric response.¹² As an interesting alternative, *Escherichia coli* (*E. coli*) also presents two advantages when utilized as template. It can guide the morphology of materials to produce rod-shaped structures and its surface can be modified by displaying proteins through genetic manipulations. In biological systems, the mineral deposition is often directed by the surface functionalization of biomolecules on insoluble organic scaffolds.¹³ The biomolecules direct the nucleation, growth, morphology and orientation of minerals around

^a State Key Laboratory of Advanced Technology for Materials Synthesis and Processing, Wuhan University of Technology, Wuhan, 430070, China. E. mail: zyfu@whut.edu.cn

^b Department of Biomaterials, Max Planck Institute of Colloids and Interfaces, Am Mühlenberg 1, 14476 Potsdam, Germany

^c Department of Physics and Astronomy, University of Missouri-Kansas City, 5110 Rockhill Road, Kansas City, Missouri 64110, USA. E. mail: chingw@umkc.edu

^d School of Chemistry, Chemical Engineering, and Life Science, Wuhan University of Technology, Wuhan, 430070, China.

^e Molecular Vista, San Jose, CA 95119, USA.

† Electronic Supplementary Information (ESI) available: [details of any supplementary information available should be included here]. See DOI: 10.1039/x0xx00000x

‡ Hang Ping and Lokendra Poudel contributed equally to this work.

scaffolds.¹⁴ For example, the oriented growth of apatite nanocrystals inside collagen fibrils in bone occurs under the actions of non-collagenous proteins,¹⁵ and the formation of complex silica patterns in diatom cell walls is also controlled by silaffin and chitin-based scaffolds.¹⁶ As a species-specific protein for the formation of diatom and spicule biosilica, catalytic enzyme silaffin and silicatein are capable of synthesizing silica *in vitro*, respectively.^{17–20} The biosilicification capabilities of silaffin functional domains or derivatives, such as R5,²¹ pentalysine,²² PL12 (KAAKLFKPKASK)²³ were widely evidenced. Solid state nuclear magnetic resonance (ssNMR)^{24,25} and sum-frequency generation (SFG) spectroscopy^{26,27} were adopted to identify the subtle change of conformation or structure of proteins during silica formation. Molecular dynamics (MD) were employed to investigate the binding of phosphorylated R5 to a silica surface through the introduction of charge and steric repulsion.²⁸ However, revealing the interfacial interactions between functional proteins and forming minerals at the atomic scale is still challenging. Recently, density functional theory (DFT) simulations have been shown to efficiently provide quantitative information of the specific interactions between interfaces at the atomic scale.^{29–32} The detailed atomic features, such as interatomic and interfacial bonding, hydrogen bonds, solvent effect, related to the interactions at interface could be clearly elucidated.^{29,30}

Here we developed a methodology where rod-shaped bacteria serve as templates for the formation of rod-shaped mesoporous silica particles. Following a biotemplating approach we designed a functionalized surface through expressing 5R5 proteins, including five repeats of R5, on the surface of cells through genetic modification.³³ The silicification preferentially occurred on the surface of *E. coli* through the interactions between 5R5 protein and tetraethyl orthosilicate (TEOS). The interfacial interactions at the atomic scale between R5 and silica were demonstrated by DFT simulations. Electrostatic interaction and hydrogen bonds contributed to the formation of rod-shaped structures. Interestingly, these structures could be transformed into mesoporous SiO_x nanorods assembled from carbon-coated nanoparticles through carbonization. The SiO_x/C composite exhibited high specific capacity, rate capability and good cycling lifetime in lithium ion batteries.

Results and discussion

Structure and composition of 5R5-silica

The silicification of genetically modified *E. coli* was prepared by sequential facile processes (Fig. S1, ESI[†]). The rod-shaped structure of mineralized samples (denoted as 5R5-silica) was retained after incubation at 37 °C for 48 hours (Fig. 1a). The rough surface indicated the deposition of silica nanoparticles (Fig. 1b). The silicon species in 5R5-silica were analyzed using cross polarization ²⁹Si MAS NMR (Fig. 1c and Fig. S2, ESI[†]). By the deconvolution of ²⁹Si CP-MAS spectrum, three Q species (Q2, Q3, Q4) were observed at -90.9, -101.4 and -112 ppm, respectively.³⁴ The ratio of Q4/Q3/Q2 was 1:1.16:0.17, indicating the high degree of silica condensation. The

coexistence of biomolecules and silica was demonstrated by the FTIR spectra (Fig. S3, ESI[†]). The two bands at 1658 cm⁻¹ and 1540 cm⁻¹ were assigned to the characteristics of amide I and II bands of biomolecules in *E. coli*, respectively. Another two peaks at 468 cm⁻¹ and 799 cm⁻¹ were corresponded to the symmetrical stretching vibration of Si-O and bending vibration of Si-OH, respectively. The sharp band at 1102 cm⁻¹ was ascribed to asymmetrical stretching vibration of Si-O-Si,³⁵ implying the formation of silica through the hydrolysis and condensation of TEOS.

In order to clearly identify the distribution of 5R5 protein and silica on the surface of 5R5-silica, photo-induced force microscope (PiFM) was employed. PiFM is an imaging technique that combines AFM tip with the spectroscopic sensitivity provided by photo-induced polarization of sample.^{36,37} The peak at 1200 cm⁻¹ resulted from C-N stretching vibration of primary amine groups of R5 peptide and was not found in the bare *E. coli* (Fig. S4, ESI[†]). Therefore, PiFM imaging was carried out using 1100 cm⁻¹ to highlight the silica and 1200 cm⁻¹ to highlight the 5R5 protein (Fig. 1d1–d4). The blue spectrum, on the feature in the topography, showed a broad peak between 1000 and 1150 cm⁻¹, which was similar to that of silica (Fig. 1e). The green spectrum showed a similar broad peak. However, it also showed a prominent peak at 1200 cm⁻¹. Therefore, this spectrum had contributions from both the silica and 5R5 protein. The combined PiFM image overlaid on the 3D topography suggested that the image taken at 1200 cm⁻¹ (red), which was an absorption peak of 5R5 protein, predominantly highlighted the edges of the features in the topography (Fig. S5, ESI[†]). The features were highlighted by the PiFM image taken at 1100 cm⁻¹ (green), which was a region of high absorption for silica. The line traces confirmed that the absorption signals at 1200 cm⁻¹ correlate to the interfaces between features on the topography (Fig. 1f–g). The location of protein on surface may facilitate the continuous silicification through interacting with surrounding TEOS.

No significant changes of the shape and diameter of rods were detected after incubation at 80 °C (Fig. S6a–c, ESI[†]). The nanoparticles were gradually observed on the surface of rods (Fig. S6d–f, ESI[†]). It may be ascribed to the extraction or dissolution of organic matrices in bacteria (Fig. S7, ESI[†]). The amorphous phase of silica was evidenced by means of XRD (Fig. S8a, ESI[†]). With increasing reaction time at 80 °C, the mass loss in mineralized samples were not much different (Fig. S8b, ESI[†]), and the coexistence of biomolecules and silica was also observed (Fig. S8c, ESI[†]). In contrast, no deposited precursor was observed on the surface of wild type cell (Fig. S9, ESI[†]). These results supported that 5R5 protein plays important roles in the formation of rod-shaped amorphous silica.

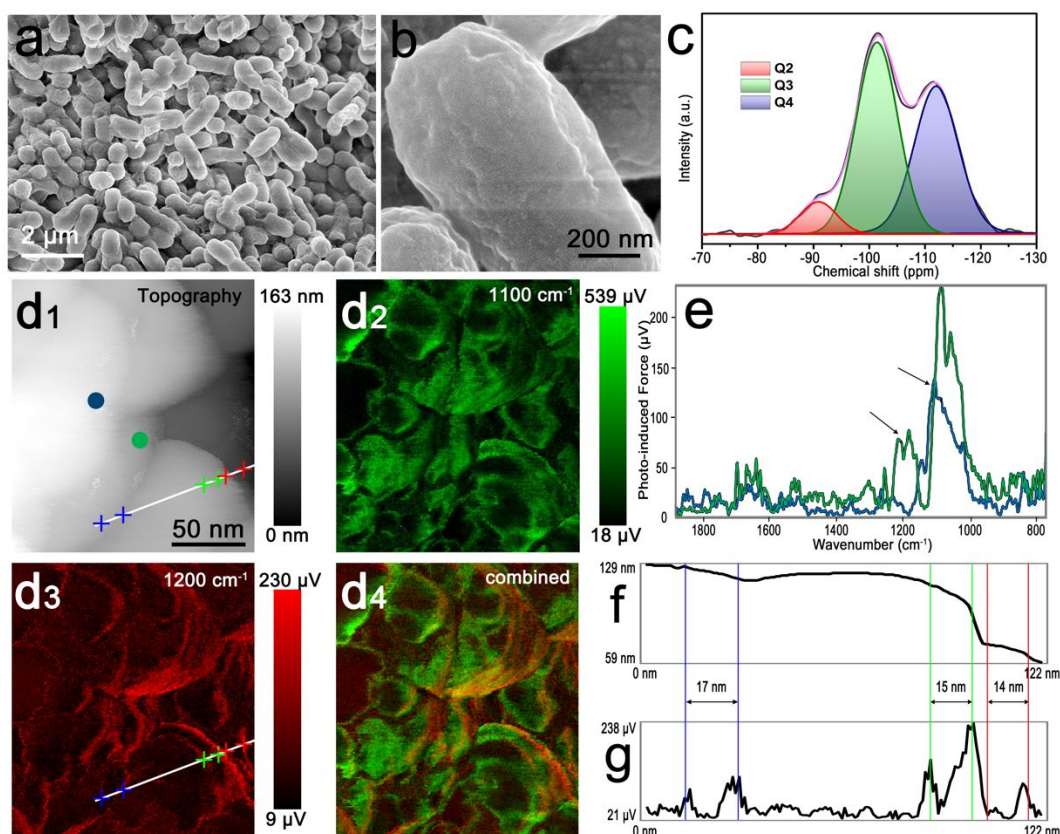


Fig. 1 Structure and composition of 5R5-silica. (a, b) SEM image. (c) ^{29}Si CP-MAS NMR spectrum. (d1) AFM topographic image, PiFM image at (d2) 1100 cm^{-1} and (d3) 1200 cm^{-1} , (d4) combined signal (color) overlaid on topography. (e) PiFM spectra of the points in (d1). (f) The line trace in (d1). (g) The line trace in (d3).

Silicification processes of genetically modified *E. coli*

The rigid rod structure indicated that the inner space of the rod-shaped structures may also be filled by silica nanoparticles. Otherwise, the structure would collapse after incubation at $80\text{ }^{\circ}\text{C}$. The silicified *E. coli* was sliced to explore the internal structure with 16 hour intervals over two days. The original *E. coli* showed rod structure with some curved shell, which was ascribed to the external force during embedding and cutting (Fig. 2a). The dark region in core may be the intracellular components. After silicification for 16 hours, the core-shell structure with rod-shape was distinctly observed in Fig. 2b. The shell was composed of nanoparticles, and some nanoparticles were dispersed inside the shell. With the increasing silicification time, the inner space was gradually filled (Fig. 2c), and transformed to a solid structure (Fig. 2d). The whole formation process is displayed in Fig. 2e. The genetically engineered cell surface, anchored by 5R5 protein, may induce the hydrolysis and condensation of TEOS through the catalytic effects of lysine group.³⁸ The silica would deposit on the surface and destroy the selective permeability of cell membrane. Afterwards, the TEOS molecules would gradually penetrate the cell membrane, and transform to silica in the inner space under the effects of intracellular 5R5 protein, which are not transported to the outer membrane timely (Fig. S10, ESI[†]).

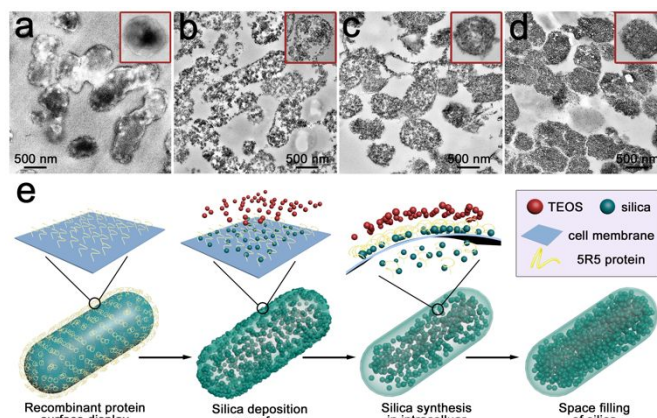


Fig. 2 The formation process of rod-shaped silica. Microtome TEM images of silicified *E. coli* at $37\text{ }^{\circ}\text{C}$ for (a) 0 h, (b) 16 h, (c) 32 h, (d) 48 h. Insets in (a-d) are the isolated transverse section of silicified *E. coli*. (e) Schematic of the biosilicification process of genetically engineered *E. coli*.

Interfacial interaction between silaffin-derived protein and silica

To explore the detailed interfacial interactions of 5R5 on the surface of *E. coli* for the formation of rod-structure, it was prudent to perform DFT-based simulation to gain useful insights to guide the silica synthesis. We constructed a large interface model using *ab initio* molecular dynamic (AIMD) to simulate the

interactions between R5 peptides and functionalized silica surfaces. The function of R5 was similar to 5R5, although it showed a slightly less capability of mineral-forming activity (Fig. S11, ESI[†]). The investigation of R5 in the DFT model cannot only represent the main characteristic of 5R5, but also decrease the complexity of simulations.

The model contained 885 atoms with periodic boundary condition for TEOS and R5 protein solvated with 50 water molecules (Fig. S12–S14, ESI[†]). The upper surface was saturated through CH₂–CH₃ to mimic the TEOS surface and the lower surface was pacified with H-atoms. For the hydration effects, we added 50 water molecules around the R5 peptide. We then constructed an initial TEOS+R5 complex model by putting R5 peptide near the lower part of the TEOS surface. After sufficient simulation time (~5 ps) for equilibrium calibration, the initial and final structures of this model are depicted in Fig. 3a–b and corresponding R5 peptide conformations are shown in Fig. 3c–d. DFT simulation demonstrated that there was a large conformation change of R5. It was clear that R5 prefers to move away from the initial surface that were terminated by Si–O–CH₂–CH₃ functional group and was attracted to the surface terminated with Si–OH group on the opposite side of the bulk SiO_x slab through periodicity of the model (Fig. 3b).

The model was fully optimized using AIMD and calculated its electronic properties (Fig. S15, ESI[†]). The calculated partial charge (PC) of the 19 individual residues in R5 are displayed in color code on the solvent excluded surface of R5 peptide (Fig. 4a). The most positively charged residue was Arg17 (+0.7628e) and the most negatively charged residue was Ser1 (-0.1158e). The total PC for R5 peptide was +2.065e. The total PC for TEOS was -2.0772e, so significant electrostatic attraction between TEOS and R5 mediated by water molecules was expected, and the interfacial amino acid was positively charged (Lys4, Arg16, Arg17). The calculated bond order (BO) vs the bond length (BL) for all interatomic pairs in the TEOS+R5 model is shown in Fig. S16. They consisted of strong covalent bonds and weaker but ubiquitous hydrogen bonds separate by bond order value of less than 0.1. We specifically identified those HBs between Si–O–R5, Si–O–water and water–R5 (Fig. 4b). It indicated that the HBs between water and R5 were the strongest and those between Si–OH–R5 were the weakest. R5 preferably attracted to the surface terminated with Si–OH group through Arg16 (O---H), Arg17 (O---H and N---H) and Leu19 (O---H) residues (Fig. 4c). These interactions synergistically contributed the conformation change of protein during silica formation.

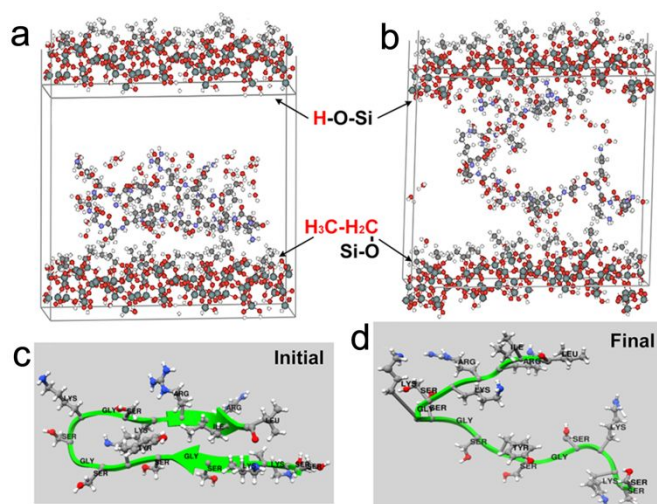


Fig. 3 The structure model of TEOS and R5 complex. (a) Initial structure of the model with periodic repetition in z direction. (b) The final relaxed structure of the model after ~5ps AIMD steps using NPT ensemble with two interfaces between TEOS and R5. (c) The initial conformation of R5 peptide and (d) the final conformation of R5 peptide. The 19 amino acid sequence in R5 (Ser-Ser-Lys-Lys-Ser-Gly-Ser-Tyr-Ser-Gly-Ser-Lys-Gly-Ser-Lys-Arg-Arg-Ile-Leu) are marked.

In the AIMD simulation, the water molecules were found to be extremely mobile and participating in dissociation as well as interfacial bonding with the protein. Detailed inspection of Fig. 4c showed signs of dissociation of H₂O molecules with concomitant formation of hydrogen bonds. Based on the simulations, we deduced that the enzymatic activity of 5R5 results from the interactions between water and lysine.^{39,40} The hydroxyl oxygen would nucleophilic attack the silicon center in TEOS, promoting the generation of Si–OH via hydrolysis.^{41,42} The Si–O–Si network was formed through the dehydration interaction between Si–OH. The result was evidenced in an anhydrous system, where no silica deposition on the surface of cell could be observed (Fig. S17, ESI[†]). Though the direct evidence of catalytic reaction between R5 and TEOS was not verified by DFT, it provided a detailed and efficient information on interactions at the interfaces at atomic scale during biosilicification. We deduced that the genetically engineered cell membrane, anchored by 5R5 protein, may attract the TEOS molecules through electrostatic interactions and induce the hydrolysis and condensation of TEOS through the catalytic effects of lysine group.^{43,44} Therefore, we assume that the C-terminal of the proteins would bind on the formed silica nanoparticles, while the N-terminal would interact with surrounding TEOS. Furthermore, the products would gradually deposit on the surface to form a rigid shell and TEOS molecules gradually penetrate the cell membrane, and transform to silica in the inner space under the effects of intracellular 5R5 protein (Fig. 2e). Finally, the solid rod-shaped silica was synthesized, and it could be transformed into monodisperse SiO₂ nanorods with novel structures.

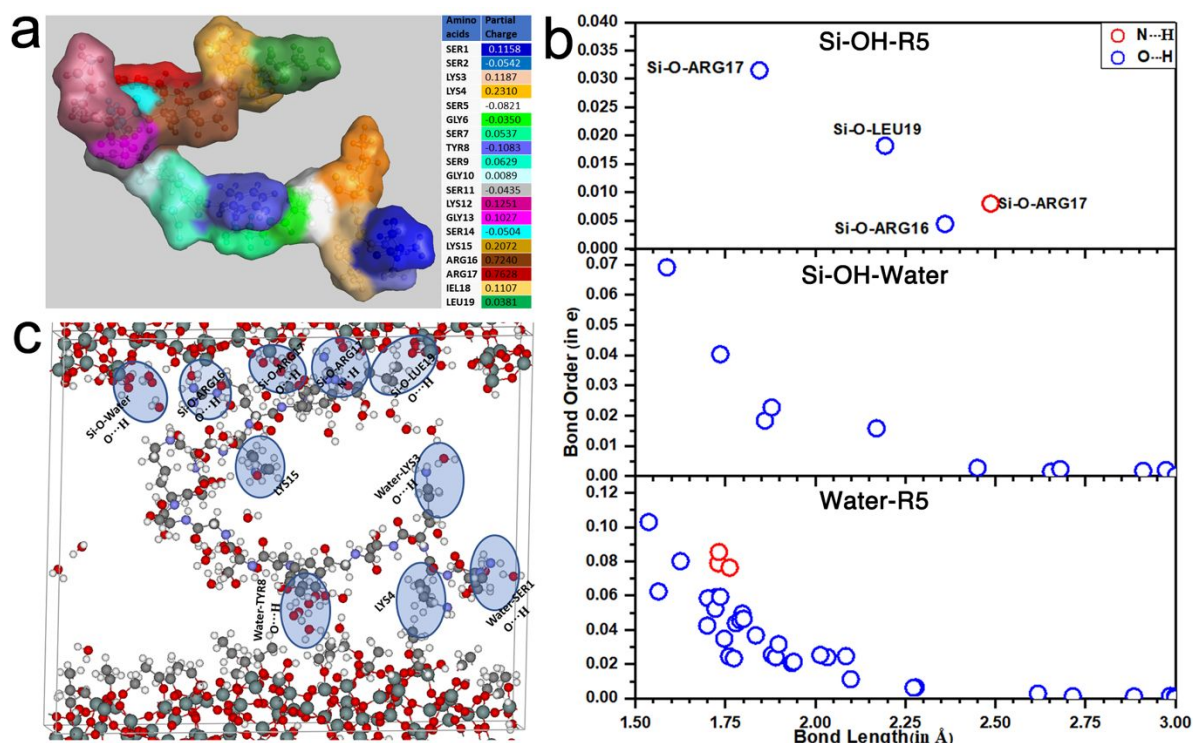


Fig. 4 The electronic properties and interatomic bonding of TEOS and R5 complex. (a) The color coded partial charge distribution with solvent excluded surface in R5 peptide. (b) Interfacial hydrogen bonding in TEOS+R5 complex. (c) Schematic of interfacial hydrogen bonding in the final structure.

Structure of SiO_x/C nanorods

After calcination at 800 °C in air, SiO_x nanorods composed of nanoparticles with a mean diameter of 10 nm were obtained (Fig. 5a and Fig. S18a-c, ESI[†]). In comparison with the precursor-coated cells, there was slight shrinkage due to the decomposition of biomolecules. From nitrogen adsorption-desorption isotherm, a representative type IV curve with a high relative pressure (P/P_0) between 0.8 to 1.0 indicated the mesoporous structures (Fig. S18d, ESI[†]). The pore size was mainly around 8 nm based on BJH model (Fig. S18e, ESI[†]). The specific surface area of 182 m² g⁻¹ was calculated by the BET method, the linear approximation of BET analysis was shown in (Fig. S18f, ESI[†]). The microtome TEM images indicated the coherent porous structure throughout the nanorods (Fig. 5b-c). The particle size between the interior and exterior region was identical from the central region of a transverse section (Fig. 5c). In contrast, the rod structure collapsed in wild type cells after heat treatment (Fig. S19, ESI[†]).

Through carbonization in inert atmosphere, the rod-shape of carbon-coated SiO_x (SiO_x/C) was preserved (Fig. S20, ESI[†]). There were no significant changes of the particle size between SiO_x and SiO_x/C (Fig. 5d). Both samples exhibited non-crystalline characteristics in XRD patterns, and the impurity phase or characteristic band of SiC was not observed in SiO_x/C (Fig. S21a-b, ESI[†]). The SiO_x nanoparticles were coated by an

amorphous carbon layer (Fig. 5e). EDS mapping confirmed the uniform distribution of Si, O, C and N elements (Fig. 5f). The carbon content in the SiO_x/C sample was about 26 wt%, evaluated by thermogravimetric analysis (Fig. S21c, ESI[†]). The Raman spectra of SiO_x/C exhibited two characteristic peaks at 1350 cm⁻¹ and 1580 cm⁻¹, corresponding to the disorder D-band and graphitic G-band of carbon, respectively (Fig. S21d, ESI[†]).⁴⁵ It was reasonable that the C and N elements were both originating from organic matrices in *E. coli*. The high-resolution C 1s core level spectrum showed three component peaks at 284.2 eV, 285.4 eV and 286.2 eV, corresponding to C-C, C-N and C-O groups, respectively (Fig. 5g and Fig. S22, ESI[†]).⁴⁶ The high-resolution N 1s spectrum exhibited two distinct peaks, pyridinic N at 398.0 eV and pyrrolic N at 400.3 eV (Fig. 5h).^{47,48} The absence of graphitic N in carbon coating indicated that the nitrogen atoms all occupied the defect sites with dangled electron pairs in carbon.⁴⁹ The N element was absent in SiO_x samples, which confirmed the incorporation of N atoms into carbon coating. The BET surface area of SiO_x/C was determined as 220 m² g⁻¹, and the type IV curves meant the mesoporous structure (Fig. 5i) and the pore size in SiO_x/C was distributed at 7 nm, slightly smaller than that of SiO_x (Fig. S18e, ESI[†]). This was due to the presence of carbon coating filling the gap between nanoparticles.

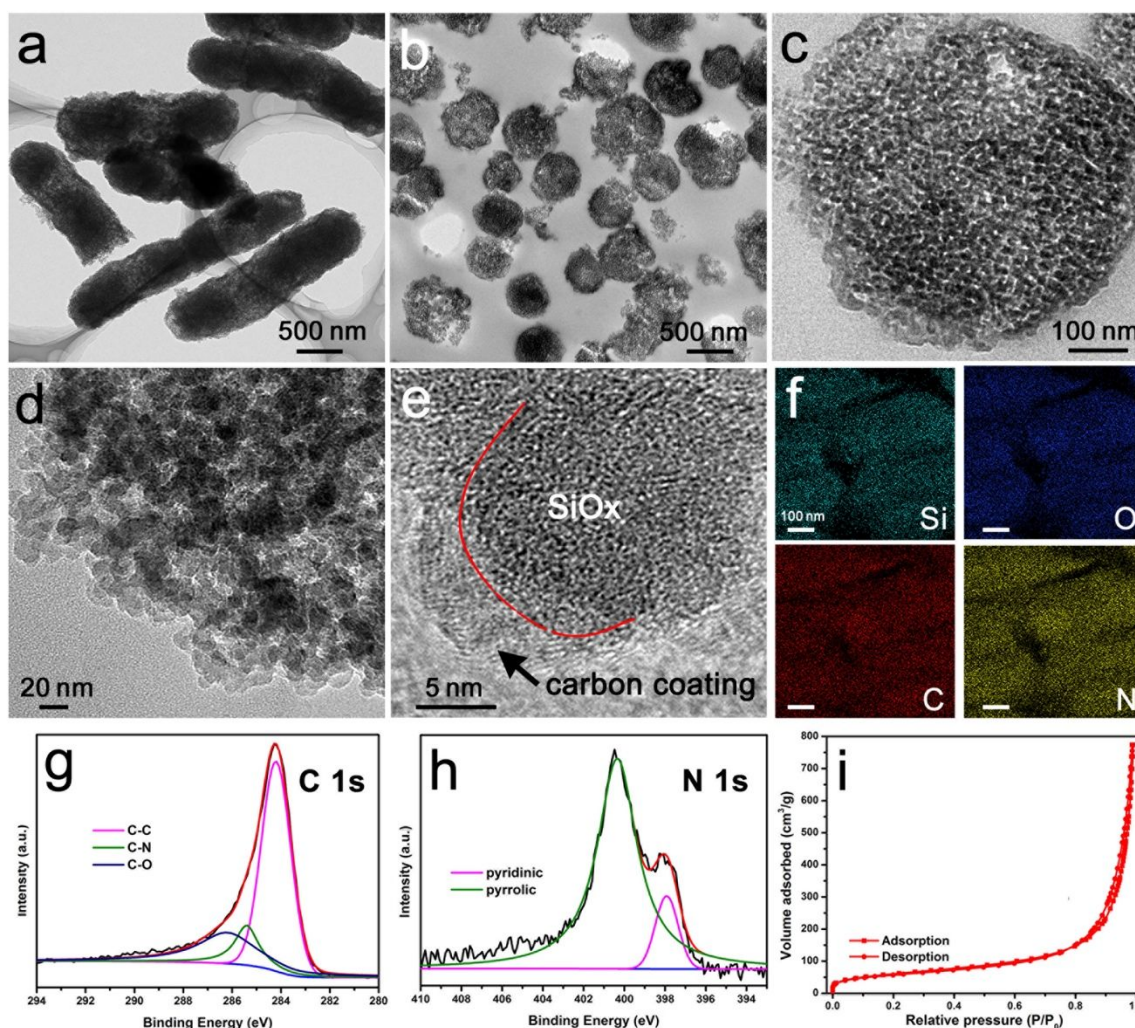


Fig. 5 Structure characterization of porous SiOx and SiOx/C nanorods. (a) TEM image of SiOx, (b-c) microtome TEM images of SiOx, (d) TEM images of SiOx/C, (e) TEM image of carbon coating, (f) elemental mapping of SiOx/C. High-resolution XPS spectra of (g) C 1s and (h) N 1s. (i) N₂ adsorption-desorption isotherms of SiOx/C and (i inset) pore size distribution.

Lithium storage of nanostructured SiOx/C

Due to the unique structure of SiOx/C, its electrochemical performance was investigated by using it as anode for lithium-ion batteries. In the first lithiation process, the sharp peak near 0 V was ascribed to the formation of Li_xSi due to the alloying reaction between Si and lithium (Fig. 6a). The broad peak at about 0.65 V corresponded to the decomposition of electrolyte and the formation of solid electrolyte interface (SEI) layers.⁵⁰ In the following cycles, the CV curves were almost overlapping, signifying the well reversible stability of SiOx/C electrode. The rate capability of SiOx-based anodes was investigated by increasing the current rates from 0.1 to 5 A g⁻¹ (Fig. 6b). The discharge capacities of SiOx/C are 994.9, 943.7, 797.2, 663.2, 544.5, and 416.1 mA h g⁻¹ at each rates, were higher than those of SiOx and commercial silica (Com-SiO₂). After being cycled at high rate of 5 A g⁻¹, the SiOx/C anode could recover to 675.6 mAh g⁻¹ at 1 A g⁻¹. The cycling behavior of these electrodes at the current rate of 1 A g⁻¹ was carried out after undergoing rate cycles. The specific capacity of SiOx/C was determined to be 791.7 mAh g⁻¹ after 100 cycles. The structure robustness of

SiOx/C was demonstrated through post-mortem after 100 cycles at 1 A g⁻¹, which determined its high reversible capacity and rate capability (Fig. S23, ESI[†]).

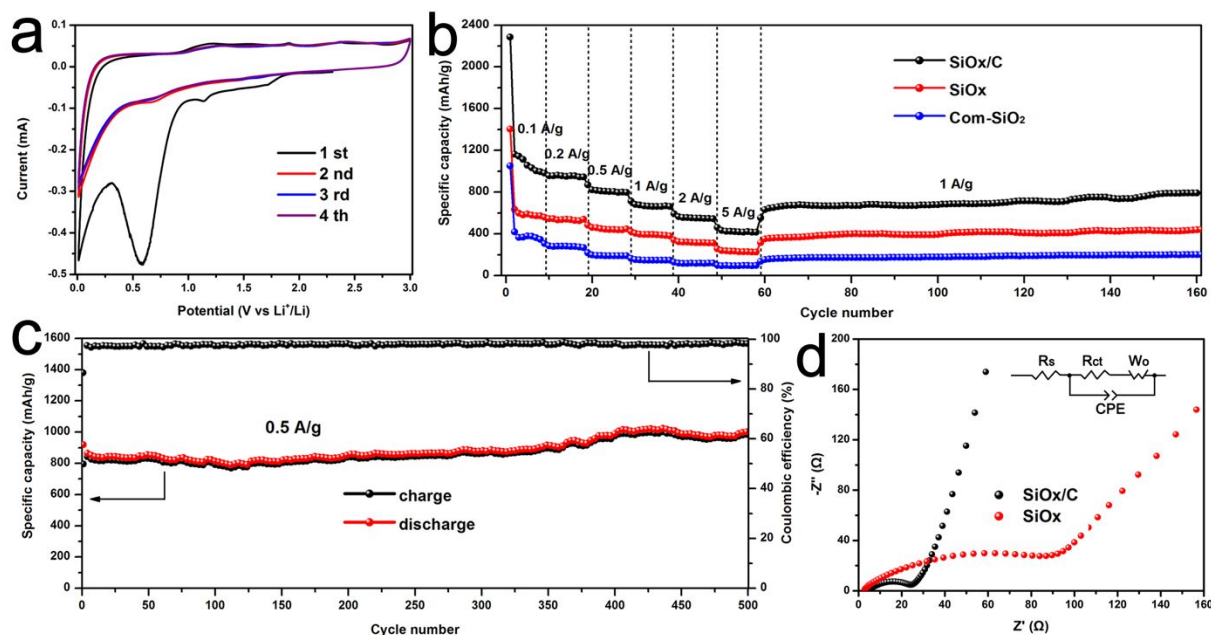


Fig. 6 Electrochemical performance of nanostructured SiOx/C electrode. (a) Cyclic voltammetry curves of SiOx/C anode at a scan rate of 0.5 mV s⁻¹. (b) Rate capability of SiOx-based electrodes at various current rates and cycling performance at a current rate of 1 A g⁻¹. (c) Long-life cycling performance of SiOx/C anode at a current rate of 0.5 A g⁻¹. (d) Nyquist plots of SiOx/C and SiOx electrodes, inset is the equivalent circuit.

The structural advantage of SiOx/C was also confirmed by the long-life cycles at higher current rates. SiOx/C electrode showed a slight rising trend of capacity, and delivered a discharge capacity of 975.8 mA h g⁻¹ after 500 cycles at a current rate of 0.5 A g⁻¹ (Figure 6c). The slight uprising capacity of SiOx/C nanorods may result from the enhanced accessibility of Li⁺ ions in SiOx/C anode, and increased the lithium accommodation behavior (Fig. S24, ESI[†]).^{51,52} The SiOx/C electrode also delivered discharge capacities of 653.2, 284.5 and 205.5 mA h g⁻¹ after 500 cycles at 2, 5 and 10 A g⁻¹, respectively (Fig. S25, ESI[†]). To the best of our knowledge, the comprehensive electrochemical performance of SiOx/C electrode was one of the best among those SiO₂-based materials (Table S1). The intrinsic difference of the transportation of Li⁺ ions and electrons was analyzed with electrochemical impedance spectroscopy (EIS) (Fig. 6d).⁵³ The equivalent circuit was presented in Figure 6d inset. Based on the fitting data, the Li⁺ apparent diffusion coefficient (D_{Li^+})⁵⁴ in SiOx/C electrode was increased to 3.38 folds higher than that of the SiOx electrode (Fig. S26, ESI[†]). The excellent electrochemical performance of SiOx/C was ascribed to its unique structure, including rod-shaped structure assembled by nanoparticles, a coherent mesoporous structure and N-doped carbon coating. The nanosized particles shorten the transportation path of Li⁺ ions, which increased the lithium storage capacity compared with the bulk electrode. In addition, the porosity structure provides abundant channels for Li⁺ ions diffusion, and maintains the structural stability through accommodating the volume variations during lithiation-delithiation processes. The highly efficient transport of electrons and Li⁺ ions is realized through

the N-doped carbon coating on nanoparticles, which is vital for improving the rate capability under high current rates.

Conclusions

In summary, we adopted a biotemplating principle by displaying 5R5 proteins on the surface of *E. coli* for specific interactions with a silicification precursor. The genetically modified *E. coli* provided a three-dimensional template to regulate the synthesis of monodisperse rod-shaped silica by employing the catalytic effect of 5R5 proteins. Silica was synthesized around cells and gradually filled the inner space. DFT simulations revealed partial charge distributions, hydrogen bonds and solvent effects in the interfacial region between the R5 peptides and the silicon sources. Since the Lys4 amino residue in the N-terminal is expected to be close to TEOS through electrostatic interactions, they may provide the catalytic site for the hydrolysis of TEOS. R5 peptides preferably attract silica precursors with hydrogen bonds between Arg16, Arg17 and Leu19 residues to form the rod-shaped structures. After carbonization, the SiOx/C nanorods exhibited unique characteristics including nanoparticles, mesoporous structures and carbon coating. It showed excellent lithium storage performance through accelerating Li⁺ ion and electron diffusion and maintained structural stability, and delivered a specific capacity of 975.8 mA h g⁻¹ after 500 cycles at a current rate of 0.5 A g⁻¹. By this approach, we could demonstrate that understanding and utilizing interfacial interactions between biomolecules and forming-minerals is a prerequisite to facilitate bioprocess-inspired synthesis of novel monodisperse structures with advanced functionality.

Experimental Section

Genetic modification of *E. coli* and 5R5 protein expression. The bacterial cell-surface display operation was performed similar as previously shown.³³ The plasmid vector of pET28a(+) (Novagen, Germany) with kana resistance was chosen. The recombinant protein 5R5 was genetically constructed and displayed on the surface through the function of carrier proteins, ice nucleation proteins (INP) (Fig. S1, ESI†). The expression procedure of 5R5 was performed in accordance with the pET System Manual (Novagen, Germany). R5 peptides with over 95 % purity were purchased from Shanghai Science Peptide Biological Technology Co., Ltd.

Silicification on the surface of *E. coli*. After protein expression, *E. coli* cells with 5R5 on surface were collected through centrifugation and re-suspended in 10 mL of deionized water (pH=7), followed by the addition of 2 mL of tetraethyl orthosilicate (TEOS, Sinopharm, China). The mixture was then incubated at 37 °C with gentle shaking for 48 hours. After washing and resuspension in 10 mL of deionized water, cells were subjected to mineralization at 80 °C for various hours (24 h, 32 h, 40 h). The mineralized sample was collected and dried in a lyophilizer. The wild type *E. coli* or *E. coli* with INP modified surface served as control groups.

Synthesis SiO_x and SiO_x/C nanorods. The mineralized samples were annealed in a muffle furnace and tubular furnace at 800 °C for 2 hours at a heating rate of 2 °C min⁻¹ to 350 °C and 4 °C min⁻¹ to 800 °C in air or Ar, respectively.

Characterization of SiO_x/C nanorods. X-ray diffraction (XRD) patterns were obtained by using Bruker D8 Advance diffractometer with Cu K α radiation ($V = 40$ kV, $I = 40$ mA) in the range of a diffraction angle of 2 θ -80°. Surface morphology information was revealed by field emission scanning electron microscopy (FESEM) in a Hitachi S-4800 at 5 kV. The silicon species in mineralized products were recorded on a Bruker Avance III 500WB (11.75 T) spectrometer with a commercial double resonance MAS probe at Larmor frequency of 99.34 MHz for ²⁹Si. Solid-state ²⁹Si CPMAS spectrum of products was recorded using 11362 scans with a recycle delay of 1 s. High power decoupling ²⁹Si spectrum was recorded using 2104 scans with a recycle delay of 30 s. Photo-induced force microscopy (PiFM, VistaScope, Molecular Vista), combining AFM tip and a tunable infrared laser to induce a dipole for chemical imaging, was used to probe the distribution of different species on the surface of bacteria. The IR sources were tuned to 1100 cm⁻¹ and 1200 cm⁻¹. Thermogravimetric (TG) analysis was performed in a Netzsch STA449F3 device at a heating rate of 10 °C min⁻¹ from 40 °C to 1000 °C. High resolution transmission electron microscopy (HRTEM) examination was carried out with a JEOL JEM 2100F at 200 kV equipped with an energy-dispersive spectroscopy (EDS) detector. In order to analyze the inner structure of nanorods, the samples were embedded in epoxy resin at 37 °C. Ultrathin sections were prepared by ultramicrotome in Leica EMUC7, followed by imaging with HRTEM. Specific surface area was determined in an ASAP 2020M adsorption apparatus using the Brunauer-Emmet-Teller (BET) method. The Raman spectrum was obtained in a Renishaw

InVia Raman spectrometer with excitation by Nd:YAG laser operating at 785 nm. The composition of mineralized samples was evaluated with Fourier Transform infrared spectroscopy (FTIR) using a ThermoScientific Nicolet 6700 from 4000 to 400 cm⁻¹, at a resolution of 4 cm⁻¹ with 32 scans. X-ray photoelectron spectroscopy (XPS) measurement was conducted by using a ThermoFisher Escalab250Xi.

Electrochemical measurements. The electrochemical performance of SiO_x/C was carried out in a CR2025-type coin cell with lithium metal foil as the counter electrode. The working electrode was prepared by mixing the active materials with Super P carbon black, polyvinylidene fluoride in a weight ratio of 7:2:1 in N-methyl-2-pyrrolidone (NMP, Aladdin, China) solution. The resultant slurry was pasted onto a copper foil and dried in a vacuum oven at 120 °C for 24 hours. The mass loading of active materials was about 1.0 mg cm⁻² in each electrode. The coin cells were assembled in an Ar-filled glove box with the concentrations of moisture and oxygen below 1 ppm. The electrolyte was 1 M lithium hexafluorophosphate in ethylene carbonate (EC)/diethyl carbonate (DEC) (1:1 v/v), and the separator was Celgard polypropylene. The galvanostatic charge/discharge experiments were carried on using a LAND battery tester CT2001A with a voltage window of 0.01-3 V (vs. Li⁺/Li) at various current densities. Cyclic voltammetric (CV) test was performed in an electrochemical workstation with 0.01-3 V (vs. Li⁺/Li) at a scanning rate of 0.5 mV s⁻¹. The electrochemical impedance spectroscopy (EIS) analysis was conducted using Autolab PGSTAT 302N equipment with the frequency range from 100 kHz to 0.01 Hz.

Theory and modelling section: methods used. We employed two ab initio quantum mechanical DFT methods to study the structural and electronic properties of the TEOS+R5 model. One was Vienna ab initio simulation package (VASP)⁵⁵ and the other was the in-house developed all electron orthogonal linear combination of atomic orbitals (OLCAO) method.⁵⁶ VASP was used for structural relaxation and AIMD. In the present study, we used the projector augmented wave (PWA) method with the Perdue-Burke-Ernzerhof (PBE) potential for exchange correlation functional within the generalized gradient approximation (GGA). For electronic relaxation, a relatively high energy cutoff of 600 eV was adopted with the electronic convergence criterion set at 10⁻⁵ eV. For each ionic relaxation step, the force convergence criteria were set to be at 10⁻³ eV/Å. Since a large periodic supercell was used, a single *k*-point calculation at zone center was sufficient. The OLCAO method was used to calculate the electronic structure and interatomic bonding. It was extremely efficient and versatile for large complex systems due to the flexible choice of the basis set. In the present calculation, a full basis (FB), which consisted of the core orbitals, occupied valence orbitals, and the next empty shell of unoccupied orbitals for each atom, was used for the determination of the self-consistent potential and the minimal basis (MB) was used for interatomic bonding calculation.

Model construction. We started the modelling of TEOS-R5 from the 162-atoms of α -SiO₂ model.⁵⁷ This was a very unique periodic model since it contained no under- or over-coordinated Si or O atoms, making it an ideal continuous

random network structure for a-SiO₂. Firstly, we constructed 3*1*1 supercell (Fig. S12, ESI[†]) and chopped it at the center along y-axis. After chopping, there were many dangling bonds of O-atoms on both lower and upper surface. The upper surface was saturated through CH₂-CH₃ to mimic the TEOS surface and the lower surface was pacified with H-atoms. This construction enabled us to construct a 3D simulation box with periodic boundary condition containing a reasonable number of atoms for ab initio molecular dynamic (AIMD) simulation. The amino acids sequence of R5 peptide was taken from Ref. 17 and the initial conformation of protein was determined by PEP-FOLD Server⁵⁸ as shown in Fig. S13. For the hydration effects, we added 50 water molecules around the R5 peptides. We then constructed an initial TEOS+R5 complex model by putting R5 peptides near the lower part of the TEOS surface (Fig. S14, ESI[†]). The entire simulation box contained a total of 885 atoms, an unprecedented size for AIMD simulations.

We used AIMD as implemented in VASP in the NPT ensemble (fixed volume and atoms) with sufficient simulation time (~5ps) for equilibrium calibration. The initial and final structures were shown in Fig. 3a and 3b with doubled cell in the c direction to better depict the interfacial structure. The final interfacial structure between R5 protein and functionalized SiOx surface at T=310 K was determined (Fig. 3b). It showed a large deformation of the protein with amino acids sequence from the initial structure (Fig. 3c-d). Detailed inspection of Figure 3b showed signs of dissociation of H₂O molecules with concomitant formation of hydrogen bonds (HBs). It was also clear that the protein preferred to move away from the initial surface that were terminated by Si-O-CH₂-CH₃ functional group and was attracted to the surface terminated with Si-O-H group on the opposite side of the initial bulk SiOx slab through periodicity of the model (Fig. 3b).

Insights from DFT. The main insights obtained from the exploratory DFT simulation was the preference of the interactions of R5 protein with TEOS-surface-functionalized with Si-OH groups over the CH₂-CH₃ groups through water molecules. The fully relaxed structure of the final interfacial model from NPT at 310K was used as input to investigate the electronic structure and bonding. The electronic structure and inter atomic bonding of the final TEOS-R5 models was summarized in Fig. S15 and S16, respectively. Since the role of DFT simulation was to provide sufficient insights for experimental synthesis and characterization of the final product, the extraneous details of these results were not included. Fig. S15 shows the calculated electronic structure in the form of density of states (DOS) and partial DOS (PDOS) for the three components of the TEOS+R5 model, water molecules, R5-peptide and TEOS. It showed that the structure was an insulator with a band gap of about 3.6 eV and the presence of an occupied defect like state from TEOS at 0.0 eV. The calculated bond order (BO) vs. the bond length (BL) for all interatomic pairs in the TEOS+R5 model is shown in Fig. S16. More detailed analysis showed evidence of ionic dissociation at the interface after AIMD simulation, which is represented in Fig. 4c.

Contributions

Zhengyi Fu, Wai-Yim Ching and Peter Fratzl provide the idea and design the structure of the work. Hang Ping and Weijian Fang perform the genetically engineering of bacteria and material synthesis. Hao Xie performs the information of proteins. Zhaoyong Zou and Pengcheng Zhai develop the synthesis approaches. Weimin Wang and Hao Wang fabricate the lithium ion battery devices. Padraic O'Reilly carries out the PiFM analysis. Lokendra Poudel and Wai-Yim Ching contribute the DFT simulations. Hang Ping, Wolfgang Wagermaier and Zhengyi Fu write and revise the paper. All authors discuss the results and comment on the paper.

Conflicts of interest

There are no conflicts to declare.

Acknowledgements

This work was financially supported by the National Natural Science Foundation of China (51521001, 51832003, 31771032), awarded by the National Natural Science Foundation of China. This research used the resources of NERSC supported by the Office of Science of DOE under contract No.DE-AC03-76SF00098 and the computing resource of Bio-consortium of the University of Missouri. We acknowledge Miss Ting-ting Luo (Center for Materials Research and Analysis, Wuhan University of Technology) for her help in HRTEM analysis. We are grateful to Bi-Chao Xu and An-Na Du of the Core Facility and Technical Support, Wuhan Institute of Virology for their technical support in sample embedding.

Notes and references

- 1 W. Li, J. Liu, D. Zhao, *Nat. Rev. Mater.*, 2016, **1**, 16023.
- 2 Z. Teng, W. Li, Y. Tang, A. Elzatahry, G. Lu, D. Zhao, *Adv. Mater.*, 2019, **31**, 1707612.
- 3 A. Kuijk, A. Blaaderen, A. Imhof, *J. Am. Chem. Soc.*, 2011, **133**, 2346-2349.
- 4 M. Eder, A. Shahrour, P. Fratzl, *Science*, 2018, **362**, 543-547.
- 5 J. Xie, H. Ping, T. N. Tan, L. W. Lei, H. Xie, Z. Fu, *Prog. Mater. Sci.*, 2019, **105**, 100571.
- 6 D. Opdenbosch, G. Fritz-Popovski, W. Wagermaier, O. Paris, C. Zollfrank, *Adv. Mater.*, 2016, **28**, 5235-5240.
- 7 O. Paris, I. Burgert, P. Fratzl, *MRS Bull.*, 2010, **35**, 219-225.
- 8 X. Wu, A. Erbe, D. Raabe, H. Fabritius, *Adv. Funct. Mater.*, 2013, **23**, 3615-3620.
- 9 J. H. Lee, C. M. Warner, H. E. Jin, E. Barnes, A. R. Poda, E. J. Perkins, S. W. Lee, *Nat. Protoc.*, 2017, **12**, 1999-2013.
- 10 P. Chen, X. Dang, M. T. Klug, N. M. D Courchesne, J. Qi, M. N. Hyder, A. M. Belcher, P. T. Hammond, *Chem. Mater.*, 2015, **27**, 1531-1540.
- 11 D. Oh, J. Qi, B. Han, G. Zhang, T. J. Carney, J. Ohmura, Y. Zhang, Y. Shao-Horn, A. M. Belcher, *Nano Lett.*, 2014, **14**, 4837-4845.
- 12 S. Kilper, T. Jahnke, M. Aulich, Z. Burghard, D. Rothenstein, J. Bill, *Adv. Mater.*, 2019, **31**, 1805597.
- 13 M. L. Zeng, Y. Y. Kim, C. Anduix-Canto, C. Frontera, D. Laundy, N. Kapur, H. K. Christenson, F. C. Meldrum, *Proc. Natl. Acad. Sci. USA*, 2018, **115**, 7670-7675.

- 14 C. J. Stephens, S. F. Ladden, F. C. Meldrum, H. K. Christenson, *Adv. Funct. Mater.*, 2010, **20**, 2108-2115.
- 15 J. Mahamid, B. Aichmayer, E. Shimon, R. Zibat, C. Li, S. Siegel, O. Paris, P. Fratzl, S. Weiner, L. Addadi, *Proc. Natl. Acad. Sci. USA*, 2010, **107**, 6316-6321.
- 16 E. Brunner, R. Richtig, H. Ehrlich, S. Paasch, P. Simon, S. Ueberlein, K. H. van Pee, *Angew. Chem. Int. Ed.*, 2009, **48**, 9724-9727.
- 17 N. Kroger, R. Deutzmann, M. Sumper, *Science*, 1999, **286**, 1129-1132.
- 18 N. Kroger, S. Lorenz, E. Brunner, M. Sumper, *Science*, 2002, **298**, 584-586.
- 19 I. Zlotnikov, P. Werner, H. Blumtritt, A. Graff, Y. Dauphin, E. Zolotoyabko, P. Fratzl, *Adv. Mater.*, 2014, **26**, 1682-1687.
- 20 V. Schoeppler, E. Reich, J. Vacelet, M. Rosenthal, A. Pacureanu, A. Rack, P. Zaslansky, E. Zolotoyabko, I. Zlotnikov, *Sci. Adv.*, 2017, **3**, eaao2047.
- 21 L. Senior, M. P. Crump, C. Williams, P. J. Booth, S. Mann, A. W. Perriman, P. Curnow, *J. Mater. Chem. B*, 2015, **3**, 2607-2614.
- 22 N. Poulsen, A. Scheffel, V. C. Sheppard, P. M. Chesley, N. Kroger, *J. Biol. Chem.*, 2013, **288**, 20100-20109.
- 23 Y. Geiger, H. E. Gottlieb, U. Akbey, H. Oschkinat, G. Goobes, *J. Am. Chem. Soc.*, 2016, **138**, 5561-5567.
- 24 A. Jantschke, E. Koers, D. Mance, M. Weingarh, E. Brunner, M. Baldus, *Angew. Chem. Int. Ed.*, 2015, **54**, 15069-15073.
- 25 A. Roehrich, G. Drobny, *Acc. Chem. Res.*, 2013, **46**, 2136-2144.
- 26 H. Lutz, V. Jaeger, L. Schmuser, M. Bonn, J. Pfaendtner, T. Weidner, *Angew. Chem. Int. Ed.*, 2017, **56**, 8277-8280.
- 27 J. E. Baio, A. Zane, V. Jaeger, A. M. Roehrich, H. Lutz, J. Pfaendtner, G. P. Drobny, T. Weidner, *J. Am. Chem. Soc.*, 2014, **136**, 15134-15137.
- 28 K. G. Sprenger, A. Prakash, G. Drobny, J. Pfaendtner, *Langmuir*, 2018, **34**, 1199-1207.
- 29 A. Rimola, M. Aschi, R. Orlando, P. Ugliengo, *J. Am. Chem. Soc.*, 2012, **134**, 10899-10910.
- 30 L. Poudel, C. Tamerler, A. Misra, W. Y. Ching, *J. Phys. Chem. C*, 2017, **121**, 28354-28363.
- 31 L. Poudel, N. F. Steinmetz, R. H. French, V. A. Parsegian, R. Podgornik, W. Y. Ching, *Phys. Chem. Chem. Phys.*, 2016, **18**, 21573-21585.
- 32 L. Poudel, R. Twarock, N. F. Steinmetz, R. Podgornik, W. Y. Ching, *J. Chem. Phys. B*, 2017, **121**, 6321-6330.
- 33 H. Ping, H. Xie, M. Xiang, B.-L. Su, Y. C. Wang, J. Y. Zhang, F. Zhang, Z. Y. Fu, *Chem. Sci.*, 2016, **7**, 6330-6336.
- 34 L. N. Niu, K. Jiao, Y. P. Qi, C. K. Y. Yiu, H. Ryou, D. D. Arola, J. H. Chen, L. Breschi, D. H. Pashley, F. R. Tay, *Angew. Chem. Int. Ed.*, 2011, **50**, 11688-11691.
- 35 R. Fu, K. Zhang, R. P. Zaccaria, H. Huang, Y. Xia, Z. Liu, *Nano Energy*, 2017, **39**, 546-553.
- 36 J. Jahng, D. A. Fishman, S. Park, D. B. Nowak, W. A. Morrison, H. K. Wickramasinghe, E. O. Potma, *Acc. Chem. Res.*, 2015, **48**, 2671-2679.
- 37 K. L. Gu, Y. Zhou, W. A. Morrison, K. Park, S. Park, Z. Bao, *ACS Nano*, 2018, **12**, 1473-1481.
- 38 H. Xu, Y. Wang, X. Ge, S. Han, S. Wang, P. Zhou, H. Shan, X. Zhao, J. Lu, *Chem. Mater.*, 2010, **22**, 5165-5173.
- 39 T. M. Davis, M. A. Snyder, J. E. Krohn, M. Tsapatsis, *Chem. Mater.*, 2006, **18**, 5814-5816.
- 40 L. Sudheendra, A. R. Raju, *Mater. Res. Bull.*, 2002, **37**, 151-159.
- 41 D. Kisailus, Q. Truong, Y. Amemiya, J. C. Weaver, D. E. Morse, *Proc. Natl. Acad. Sci. USA*, 2006, **103**, 5652-5657.
- 42 R. L. Brutchey, E. S. Yoo, D. E. Morse, *J. Am. Chem. Soc.*, 2006, **128**, 10288-10294.
- 43 S. Wang, X. Ge, J. Xue, H. Fan, L. Mu, Y. Li, H. Xu, J. R. Lu, *Chem. Mater.*, 2011, **23**, 2466-2474.
- 44 Z. S. Al-Garawi, J. R. Thorpe, L. C. Serpell, *Angew. Chem. Int. Ed.*, 2015, **54**, 13327-13331.
- 45 D. Chao, C. Zhu, P. Yang, X. Xia, J. Liu, J. Wang, X. Fan, S. V. Savilov, J. Lin, H. J. Fan, Z. X. Shen, *Nat. Commun.*, 2016, **7**, 12122.
- 46 R. Hao, Y. Yang, H. Wang, B. Jia, G. Ma, D. Yu, L. Guo, S. Yang, *Nano Energy*, 2018, **45**, 220-228.
- 47 Z. Luo, S. Lim, Z. Tian, J. Shang, L. Lai, B. MacDonald, C. Fu, Z. Shen, T. Yu, J. Lin, *J. Mater. Chem.*, 2011, **21**, 8038.
- 48 C. Yang, Y. Zhang, J. Zhou, C. Lin, F. Lv, K. Wang, J. Feng, Z. Xu, J. Li, S. Guo, *J. Mater. Chem. A*, 2018, **6**, 8039-8046.
- 49 P. Błoński, J. Tuček, Z. Sofer, V. Mazánek, M. Petr, M. Pumera, M. Otyepka, R. Zbořil, *J. Am. Chem. Soc.*, 2017, **139**, 3171-3180.
- 50 C. Tang, Y. Liu, C. Xu, J. Zhu, X. Wei, L. Zhou, L. He, W. Yang, L. Mai, *Adv. Funct. Mater.*, 2018, **28**, 1704561.
- 51 X. Zhou, L. J. Wan, Y. G. Guo, *Adv. Mater.*, 2013, **25**, 2152-2157.
- 52 Y. Cheng, Q. Li, C. Wang, L. Sun, Z. Yi, L. Wang, *Small*, 2017, **13**, 1701993.
- 53 Y. Jiang, J.-L. Yue, Q. Guo, Q. Xia, C. Zhou, T. Feng, J. Xu, H. Xia, *Small*, 2018, **14**, 1704296.
- 54 Y. Tang, Y. Zhang, X. Rui, D. Qi, Y. Luo, W. R. Leow, S. Chen, J. Guo, J. Wei, W. Li, J. Deng, Y. Lai, B. Ma, X. Chen, *Adv. Mater.*, 2016, **28**, 1567-1576.
- 55 G. Kresse and J. Furthmuller, Vienna ab-initio simulation package (VASP): The guide. VASP Group, Institut fur Materialphysik, Universitat Wien, Sensengasse, 2002.
- 56 W. Y. Ching and P. Rulis, Electronic structure methods for complex materials: The orthogonalized linear combination of atomic orbitals. Oxford Univ. Press 2012.
- 57 W. Y. Ching, *Phys. Rev. Lett.*, 1981, **46**, 607-609.
- 58 Y. Shen, J. Maupetit, P. Derreumaux and P. Tuffery, *J. Chem. Theory Comput.*, 2014, **10**, 4745-4758.

Table of Contents

A biotemplating principle was adopted to display silaffin-derived protein on the surface of *Escherichia coli* for producing monodisperse rod-shaped silica.

